Attack Intent Inference of Hypersonic Glide Vehicle Based on a Unified Dynamics and Decision-Making Model

YOUNGIM NAM, Graduate Student Member, IEEE

HOJIN LEE , Student Member, IEEE

Ulsan National Institute of Science and Technology, Ulsan, South Korea

HYOEKJIN CHOI (D), Member, IEEE

Agency for Defense Development, Seoul, South Korea

WON-SANG RA , Member, IEEE Handong Global University, Pohang, South Korea

CHEOLHYEON KWON D, Member, IEEE

Ulsan National Institute of Science and Technology, Ulsan, South Korea

This article proposes an attack intent inference framework for defending against hypersonic glide vehicles (HGVs). Predicting the HGV behaviors poses significant challenges for defense systems due to their highly dynamic and erratic maneuvers. Complementing the limitations of the dynamics model, a unified dynamics and decisionmaking model of HGV is developed. First, dynamically feasible attack regions can be set by the dynamics model. Within this region, the decision-making model encodes the rational intent of attack, strategically selecting the target that maximally attains the threat value. To further address the dynamical uncertainties and potential discrepancies from the rational decision-making model, a proximity parameter is introduced in light of the maximum entropy principle. The attack intent of the HGV is then inferred by the Bayesian approach, whereby recursively updates the probability of the potential target

Received 31 January 2025; revised 9 May 2025; accepted 20 May 2025. Date of publication 29 May 2025; date of current version 13 October 2025.

DOI. No. 10.1109/TAES.2025.3575052

Refereeing of this contribution was handled by Q. Zhu.

This work was supported by the Agency For Defense Development by the Korean Government under Grant UI247003TD.

Authors' addresses: Youngim Nam, Hojin Lee, and Cheolhyeon Kwon are with the Department of Mechanical Engineering, Ulsan National Institute of Science and Technology, Ulsan 44919, South Korea, E-mail: (nyi0944@unist.ac.kr; hojinlee@unist.ac.kr; kwonc@unist.ac. kr); Hyoekjin Choi is with the Command and Control Systems PMO, Agency for Defense Development, Seoul 305-600, South Korea, E-mail: (mycult@add.re.kr); Won-sang Ra is with the Department of Mechanical and Control Engineering, Handong Global University, Pohang 37554, South Korea, E-mail: (wonsang@handong.edu). (Corresponding author: Cheolhyeon Kwon.)

0018-9251 © 2025 IEEE

to be attacked. Numerical simulations demonstrate that the proposed framework achieves superior accuracy and faster convergence in intent inference compared to existing methods, under different scenarios with varying uncertainty levels.

I. INTRODUCTION

IN recent years, hypersonic glide vehicles (HGVs) have gained increasing attention in modern warfare due to their extreme speed and highly agile maneuverability [1]. Unlike traditional ballistic missiles that follow foreseeable parabolic trajectories, HGVs exhibit erratic maneuvers, mixing longitudinal skipping and lateral weaving. These maneuvers complicate predictions of the HGV trajectory, ultimately impeding effective defense strategies [2]. For military defense systems, accurate prediction of the HGV behaviors is essential not only for successful interception but also for the optimal allocation of defense weapon

Seeking to predict the HGV behaviors and further anticipate its target, the existing research can be divided into three main categories [3]: 1) physics-based prediction; 2) maneuver mode identification; and 3) intent inference. Physicsbased approaches are principled by the aerodynamics and kinematic model of HGVs, often utilizing classical filtering techniques, such as the Kalman filter (KF) [4], [5], [6]. From the defender's standpoint, however, the specific dynamics models and guidance laws of the observed HGV remain uncertain, making its trajectory prediction inherently challenging. To address these limitations, some methods have employed parametric representations of the dynamics model, iteratively estimating unknown parameters in real time [7]. Nonetheless, physics-based approaches may suffer from significant long-term errors when confronted with sudden maneuvers, sometimes misestimating in the order of hundreds of kilometers [8].

Physics-based prediction can be augmented by maneuver mode identification, which focuses on recognizing the distinct flight maneuvers of HGVs. Longitudinal maneuvers typically include equilibrium glide and skip glide, while lateral maneuvers encompass weaving and turning [9]. Various curve-fitting techniques have been employed to distinctly model the individual maneuver dynamics from trajectory data [10], [11]. Still, the resulting models for individual maneuver modes are often insufficient to capture the nonlinearity and high dimensionality of the HGV flight data. To address the limit of model-based approaches, recent studies have resorted to data-driven approaches, such as long shortterm memory networks [12]. These methods capture temporal dependencies and nonlinear relationships, enabling more effective classification of maneuver modes [13], [14], [15]. As such, the data-driven approaches excel in short-term predictions by specifying individual maneuver characteristics. However, when it goes with long-term, unexpected transitions between maneuver modes may degrade the prediction accuracy.

The maneuver mode transition of HGVs is closely tied to the attacker's tactical objective, striking the designated target. Accordingly, attack intent inference is crucial for identifying the target to be attacked and enabling the long-term prediction of the HGV trajectory. While intent inference has been widely employed in other domains, such as combat aircraft [16], [17], [18], its applicability is relatively unexplored for HGVs. One prominent approach to intent inference is planning-based, which designs a rational decision-making model under the premise that the HGV maximizes the tactical objective cost for achieving its intent [19]. Although this method explicitly reasons out the HGV's intent, it fails when the real-world HGV does not conform to the rational model [20]. Furthermore, it typically relies on simplistic metrics (e.g., distance to the target) without a deeper consideration of dynamic information. The data-driven approach can obviate such modeling issues by directly inferring the intent from the observed HGV trajectory [3], [21]. This idea can be further advanced to end-to-end learning frameworks that directly predict the HGV's future trajectory, bypassing a separate intent inference stage [8], [22], [23]. However, the performance of the data-driven approaches hinges on the quality of available datasets, whereas the HGV flight data are hard to acquire in real warfare scenarios.

Motivated by the aforementioned drawbacks, this article proposes an attack intent inference framework by developing a unified dynamics and decision-making model for HGVs. This method infers the potential attack target in a planning-based manner while taking appropriate care of the uncertainties inherent in the both dynamics and decision-making models. First, the current state of the HGV is estimated from the observed trajectory, and potential trajectory samples are generated by propagating the state forward through the numerical integration of the stochastic HGV dynamics. These samples form the dynamically feasible region, whereby it is determined whether each target is reachable. Subsequently, the probability distribution of HGV's future state with respect to each target is computed. Based on this probability distribution, we encode the attack intent into the decision-making model, strategically selecting the target that maximizes the threat value.

On the other hand, environmental disturbances, sensor noise, or the simplified dynamics model may introduce dynamics uncertainties, and the assumption that the HGV prioritizes targets solely by threat value may not fully capture the attack intent in the real world. To address such uncertainties, the decision-making model incorporates a proximity parameter in light of the maximum entropy principle [24]. The use of proximity-based decision-making models has been widely studied in many applications, such as robotics, autonomous vehicles, and aerial platforms [20], [25], [26]. To the best of the authors' knowledge, however, this is the first attempt to apply the proximity parameter into the HGV prediction problem. This parameter handles uncertainties by evaluating how well the observed HGV behavior aligns with dynamics and the decision-making models. Finally, Bayesian inference is employed to recursively update the probability of the potential attack target with respect to the estimated proximity parameter.

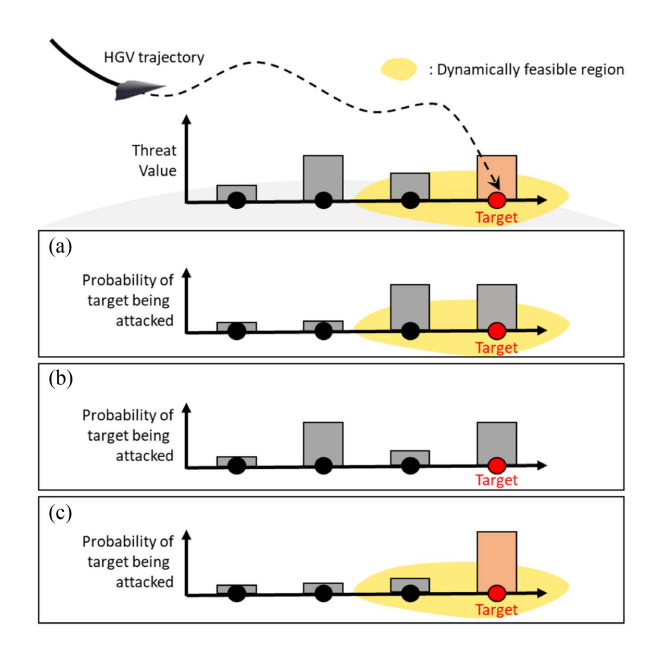


Fig. 1. Illustration of the HGV's attack scenario: (a) Dynamics-based prediction considers dynamical feasibility but overlooks tactical objectives. (b) Planning-based prediction only focuses on tactical objectives. (c) Proposed prediction integrates dynamical feasibility and tactical objectives to improve intent inference accuracy.

In summary, the proposed algorithm unifies dynamicsbased trajectory propagation with planning-based decision reasoning to facilitate precise and reliable intent inference, as illustrated in Fig. 1. By leveraging both dynamical feasibility and tactical objectives, we can complement the dynamics and the decision-making model with each other. The contributions of this article are summarized as follows.

- We propose an attack intent inference framework that integrates the dynamics and the decision-making model of HGVs, enabling precise and timely prediction of the target to be attacked.
- 2) We introduce the proximity parameter to the decision-making model, enhancing the prediction reliability in handling uncertainties.
- Numerical simulations are conducted to validate the effectiveness of the proposed algorithm compared to existing approaches, under different scenarios with varying uncertainty levels.

The rest of this article is organized as follows. Section II introduces the mathematical models, including the HGV dynamics and its parametric representations. Section III details the proposed attack intent inference framework, integrating dynamics-based prediction with the planning-based decision-making model. Numerical simulation and comparative studies are presented Section IV. Finally, Section V concludes this article.

II. PROBLEM FORMULATION

A. HGV Dynamics Model

Neglecting the effects of the Earth's oblateness and rotation, the dynamics model of HGV is described in

the velocity-turn-climb (VTC) coordinate system as follows [8], [14]:

$$\dot{x} = \begin{bmatrix} v \sin \theta \\ \frac{v \cos \theta \sin \chi}{(R_e + h) \cos \psi} \\ \frac{v \cos \theta \cos \chi}{R_e + h} \\ -\frac{D}{m} - g \sin \theta \\ \frac{L \cos \gamma}{mv} + \frac{v \cos \theta}{R_e + h} - \frac{g \cos \theta}{v} \\ \frac{L \sin \gamma}{mv \cos \theta} + \frac{v \cos \theta \sin \chi \tan \psi}{R_e + h} \end{bmatrix}$$
(1)

where state vector $x := [h, \phi, \psi, v, \theta, \chi]$ represents the altitude, longitude, latitude, velocity, flight path angle, and flight heading angle, respectively, m denotes the HGV's mass, R_e is the Earth's radius, and g is the gravity acceleration. The bank angle is denoted as γ , and L and D are the aerodynamic lift and drag, respectively, which are defined as

$$L := \frac{\rho v^2 SC_L(\alpha, Ma)}{2},$$

$$D := \frac{\rho v^2 SC_D(\alpha, Ma)}{2}$$
(2)

where C_L and C_D represent the aerodynamic lift and drag coefficient, respectively, which are functions of angle of attack α and Mach number Ma. S is the HGV's reference area, and ρ is atmospheric density which is modeled using the exponential equation [9], [27]

$$\rho = \rho_0 \exp\left(-h/h_s\right)$$

where ρ_0 is the atmospheric density at sea level, and h_s is the scale height, describing the rate of density decrease with altitude.

B. Parametric Dynamics Model

12556

As seen in (1) and (2), the states of HGV are governed by the interplay between aerodynamic forces and the guidance law's control inputs, α and γ . These interdependencies pose challenges in accurately estimating the vehicle states due to their high dimensionality and nonlinear coupling. Such a complexity can be handled by parameterizing the dynamics model [3]. This approach consolidates unknown parameters into a reduced set of composite parameters, simplifying the estimation process and enhancing computational efficiency.

Based on (2), the aerodynamic acceleration in the VTC coordinate system can be expressed as follows [13]:

$$a_{1} = -\frac{\rho v^{2} S C_{D}(\alpha, Ma)}{2m}$$

$$a_{2} = \frac{\rho v^{2} S C_{L}(\alpha, Ma)}{2m} \sin \gamma$$

$$a_{3} = \frac{\rho v^{2} S C_{L}(\alpha, Ma)}{2m} \cos \gamma$$
(3)

where a_1 , a_2 , and a_3 , respectively, represent the aerodynamic accelerations in the velocity, turn, and climb directions. Here, $\rho v^2/2$ is a state-dependent variable that

is generally observable via various sensor measurements.¹ However, other critical parameters, such as the dynamics model variables (S, m), aerodynamics coefficients (C_D, C_L) , and control inputs (α, γ) remain unobservable. Since these are crucial for accurately predicting the HGV's states, they must be estimated online.

To reduce dimensionality and handle the coupling among these unknowns, we regroup them into the composite parameters $u := [u_1, u_2, u_3]$ as the control state to be estimated, each defined as

$$u_{1} := \frac{SC_{D}(\alpha, Ma)}{m}$$

$$u_{2} := \frac{SC_{L}(\alpha, Ma)}{m}$$

$$u_{3} := \gamma.$$
(4)

By substituting (4) into (1), the dynamics model of HGVs can be reformulated with the augmented state vector $X := [h, \phi, \psi, v, \theta, \chi, u_1, u_2, u_3]$

$$\dot{X} = f(X) = \begin{bmatrix}
v \sin \theta \\
\frac{v \cos \theta \sin \chi}{(R_e + h) \cos \psi} \\
\frac{v \cos \theta \cos \chi}{R_e + h} \\
-\frac{\rho v}{2} u_1 - g \sin \theta \\
\frac{\rho v}{2} u_2 \cos u_3 + \frac{v \cos \theta}{R_e + h} - \frac{g \cos \theta}{v} \\
\frac{\rho v}{2 \cos \theta} u_2 \sin u_3 + \frac{v \cos \theta \sin \chi \tan \psi}{R_e + h}
\end{bmatrix}$$

$$w_1 \\
w_2 \\
w_3$$
(5)

where $w = [w_1, w_2, w_3] \sim \mathcal{N}(0, \Sigma_w)$ is a zero-mean white noise vector, introduced to account for the dynamic uncertainties associated with the control state u. Every moment the measurement is acquired, these states are iteratively estimated using a nonlinear filtering approach, such as the Cubature KF (CKF) [28].

III. ALGORITHM DEVELOPMENT

The proposed algorithm consists of three main modules: 1) dynamics-based prediction; 2) planning-based prediction; and 3) attack intent inference. Fig. 2 provides an overview of the proposed algorithm.

A. Dynamics-Based Prediction

To utilize dynamics information in attack intent inference, the proposed algorithm first predicts the probability distribution of future states using the dynamics model. At time step t, the estimated state is assumed to follow a normal distribution

$$\hat{X}^t \sim \mathcal{N}(\mu_X^t, \Sigma_X^t) \tag{6}$$

¹In this article, we assume that the HGV's state x is obtained through the postprocessing of radar measurements with Gaussian noise as $\mathcal{N}(0, \sigma^2)$ [8].

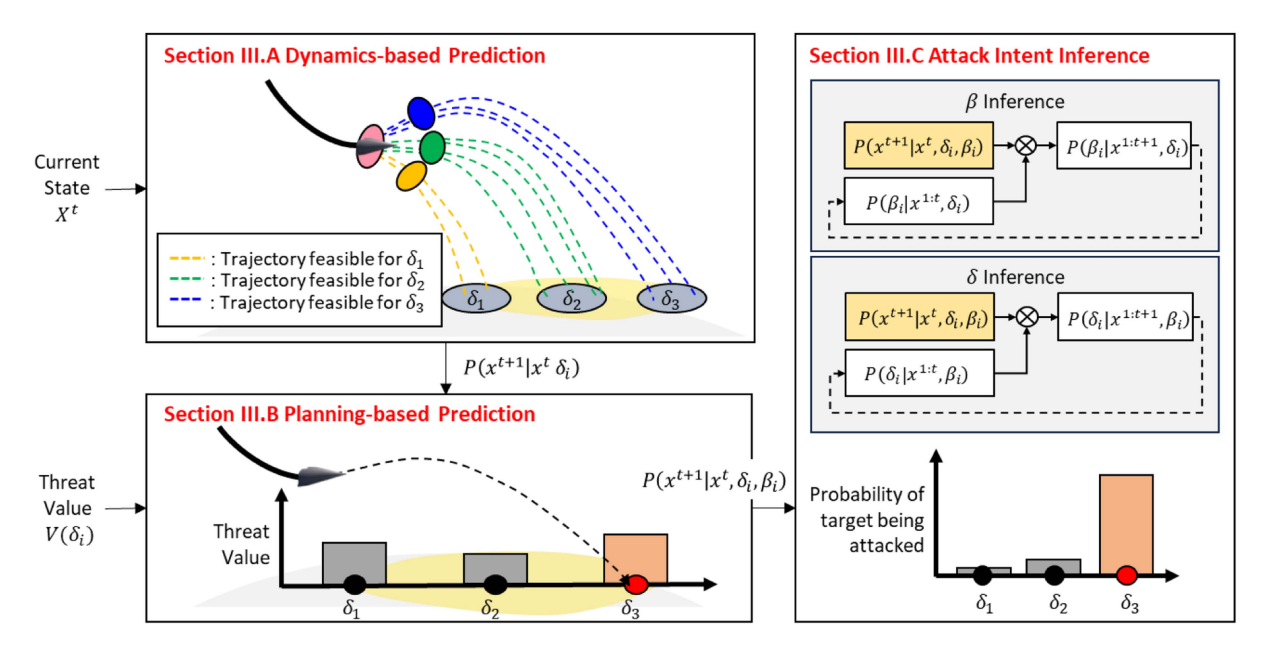


Fig. 2. Overall architecture of the proposed attack intent inference framework with the unified dynamics and decision-making model.

where μ_X^t and Σ_X^t , respectively, represent the mean and covariance of the estimated state. To generate potential future trajectories propagating from time step t, Monte Carlo (MC) simulations are performed with different initial states sampled by (6). Although the generated trajectory samples comply with dynamics model (5), they may not adequately reflect the variation of control inputs (u_1, u_2, u_3) that are more subject to the attacker's intent. In particular, the bank angle γ (i.e., u_3) can undergo substantial shifts momentarily, allowing the HGV to execute abrupt turns and reach distant targets. Consequently, relying solely on the dynamics model-based sampling of γ during forward propagation could underestimate the true reachable region. To better address such irregular behavior, we exceptionally sample γ from a uniform distribution over a dynamically feasible range during each MC run²

$$\gamma \sim \mathcal{U}(\gamma_{\min}, \gamma_{\max})$$
 (7)

where γ_{min} and γ_{max} represent the lower and upper bounds of the feasible bank angle range. Note that this remedy does not reshape the dynamics model, rather it algorithmically addresses exception handling.

Each sampled state from (6) and (7) is then propagated forward in time via (5) until the HGV reaches the ground. During this process, the noise terms w_1 , w_2 , and w_3 in (5) are set to zero to enable deterministic trajectory propagation and reduce computational overhead. This step yields potential trajectory samples as follows:

$$\tau_k = \{x_k^t, x_k^{t+1}, \dots, x_k^{t+T}\} \quad \forall k = 1, \dots, N_s$$
(8)

where N_s is the number of MC samples, and T represents the time step when the HGV reaches the ground.

Inspired by rejection sampling principles in MC methods [29], the proposed algorithm then prunes trajectory samples that fail to meet specific feasibility requirements. Specifically, let $\delta_i \in \{\delta_1, \delta_2, \dots, \delta_{N_\delta}\}$ be the set of potential attack targets, and define the trajectory as feasible if it terminates within the target region R_{δ_i} . The set of feasible trajectories for a target δ_i is given by

$$\mathcal{T}_i = \{ \tau_k : x_k^{t+T} \in R_{\delta_i} \} \quad \forall i = 1, \dots, N_{\delta}.$$
 (9)

By filtering out trajectories that fall outside R_{δ_i} , the algorithm ensures dynamically feasible samples for each target.

Finally, for each target δ_i , the HGV's future state probability distribution is computed by normalizing \mathcal{T}_i . Assuming a normal distribution, the predicted state at t+1 conditioned on reaching δ_i is given by

$$P(x^{t+1}|x^t, \delta_i) \sim \mathcal{N}(\mu_x^{t+1}, \Sigma_x^{t+1})$$
 (10)

where

$$\mu_x^{t+1} = \frac{1}{|\mathcal{T}_i|} \sum_{k \in \mathcal{T}_i} x_k^{t+1}$$

$$\Sigma_x^{t+1} = \frac{1}{|\mathcal{T}_i| - 1} \sum_{k \in \mathcal{T}_i} (x_k^{t+1} - \mu_x^{t+1}) (x_k^{t+1} - \mu_x^{t+1})^T. \quad (11)$$

This distribution provides the predicted mean and covariance of HGV's future state with respect to each target, which is then incorporated into the subsequent decision-making process to reflect the HGV's dynamical feasibility. The overall process of dynamics-based prediction is illustrated in Fig. 3.

 $^{^2}$ In contrast, the other parameters u_1 and u_2 typically show smaller variations over the entire flight. Detailed profiles of u are displayed in Section IV.

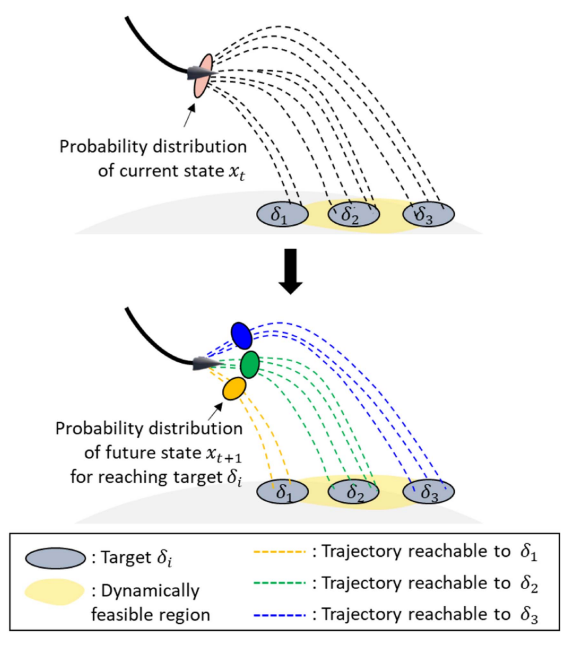


Fig. 3. Illustration of the dynamics-based prediction process.

B. Planning-Based Prediction

Extending beyond the dynamics-based prediction, we develop the decision-making model of the HGV by incorporating tactical objectives, such as the threat value $V(\delta_i)$. This threat value $V(\delta_i)$ can be defined by the defender based on available mission-level information, such as the strategic importance of facilities, population density, or military asset distribution [30]. While the attacker's true intent is not directly observable, these values serve as reasonable proxies for what a rational attacker might prioritize in order to deliver maximum damage to the defender. Accordingly, the decision-making model is designed such that the HGV strategically selects the target δ_i to maximize $V(\delta_i)$. However, this rational model, whose decision-making is solely based on the threat value $V(\delta_i)$, may not fully capture the complexities of attack intent in the real world. Furthermore, environmental disturbances, sensor noise, and simplified dynamics introduce uncertainties, further complicating accurate intent inference.

To account for these uncertainties, the decision-making model incorporates a proximity parameter $\beta \in (0, \infty)$, grounded in the maximum entropy principle [24]. This approach has proven its effectiveness in fields like robotics and autonomous systems to model decision-making processes under uncertainty [20], [26]. According to the maximum entropy principle, the state transition of the HGV forms an exponential probability distribution associated with threat value, i.e., its direction is exponentially more likely toward the target with higher $V(\delta_i)$. In this framework, the proximity parameter β enables the proposed algorithm to 1) properly update the HGV's state transition probability while ensuring dynamical feasibility; and 2) further adjust the transition probability in the presence of potential model discrepancies and dynamics uncertainties.

Building on the dynamics information from (10), the decision-making model incorporates both tactical objectives and the proximity parameter, defining the state transition probability as follows:

$$P(x^{t+1}|x^{t}, \delta_{i}, \beta_{i})$$

$$= Z^{-1} \exp\left(-\beta_{i} \cdot V(\delta_{i}) \cdot \frac{(x^{t+1} - \mu_{x}^{t+1})^{2}}{2\Sigma_{x}^{t+1}}\right)$$
(12)

where Z is a normalization constant. Consistent with (10), this probability distribution in (12) can also be expressed as a normal distribution

$$P(x^{t+1}|x^t, \delta_i, \beta_i) \sim \mathcal{N}(\bar{\mu}_x^{t+1}, \bar{\Sigma}_x^{t+1})$$

where the mean $\bar{\mu}_{\mathbf{x}}^{t+1}$ and the variance $\bar{\Sigma}_{\mathbf{x}}^{t+1}$ are defined as

$$\bar{\mu}_x^{t+1} = \mu_x^{t+1}$$

$$\bar{\Sigma}_x^{t+1} = \frac{\Sigma_x^{t+1}}{\beta_i V(\delta_i)}.$$

Notably, the parameter β_i directly modulates the covariance of state transition (12). A higher β_i results in a concentrated distribution of the HGV behavior maximizing the threat value $V(\delta_i)$, implying the decision-making model that the HGV rationally pursues the primary tactical objective. Conversely, a lower β_i leads to a dispersed distribution of the HGV behavior, allowing the inference process to accommodate the potential discrepancy in the attacker's decision-making model as well as uncertainties in the system dynamics. This decision-making model thus accounts for both the dynamics and the uncertainty inherent in the HGV's tactical behavior, serving as a basis for attack intent inference.

C. Attack Intent Inference

Under the decision-making model, the state transition probability distribution derived in (12) serves as the likelihood for intent inference. Intuitively, this likelihood reflects how well the model aligns with the observed trajectory of HGV. When new measurements x^{t+1} are obtained, Bayesian inference is performed to infer both the proximity parameter β and the target to be attacked δ . This inference is updated in a recursive manner, where the each recursion carries out the following steps.

First, the proximity parameter β_i , associated with each target δ_i , $i \in \{1, 2, ..., N_\delta\}$, is updated by the Bayes rule

$$P(\beta_i|x^{1:t+1}, \delta_i) = \frac{P(x^{t+1}|x^t, \delta_i, \beta_i)P(\beta_i|x^{1:t}, \delta_i)}{P(x^{t+1}|x^t, \delta_i)}.$$
 (13)

To ensure β_i value within the practically valid range $(0, \infty)$, the prior is modeled as a truncated normal distribution $\beta_i \sim \mathcal{TN}(\mu_{\beta_i}, \Sigma_{\beta_i}, 0, \infty)$ [31]. The corresponding probability density function at time step t is given by

$$P(\beta_{i}|x^{1:t}, \delta_{i}) = \begin{cases} \frac{\Psi(\beta_{i}; \mu'_{\beta_{i}}, \Sigma'_{\beta_{i}})}{1 - \Phi(0; \mu'_{\beta_{i}}, \Sigma'_{\beta_{i}})}, & \beta_{i} > 0\\ 0, & \beta_{i} \leq 0 \end{cases}$$
(14)

where Ψ and Φ , respectively, represent the probability density and cumulative distribution functions of the standard

normal distribution

$$\Psi\left(\beta_{i}; \mu_{\beta_{i}}^{t}, \Sigma_{\beta_{i}}^{t}\right) = \frac{1}{\sqrt{2\pi \Sigma_{\beta_{i}}^{t}}} \exp\left(-\frac{(\beta_{i} - \mu_{\beta_{i}}^{t})^{2}}{2\Sigma_{\beta_{i}}^{t}}\right)$$

$$\Phi\left(0; \mu_{\beta_{i}}^{t}, \Sigma_{\beta_{i}}^{t}\right) = \int_{-\infty}^{0} \Psi\left(\beta_{i}; \mu_{\beta_{i}}^{t}, \Sigma_{\beta_{i}}^{t}\right) d\beta_{i}.$$

Under this prior (14) and likelihood derived from (12), the posterior probability of proximity parameter $P(\beta_i|x^{1:t+1}, \delta_i)$ from (13) is represented by

$$P(\beta_{i}|x^{1:t+1}, \delta_{i}) = \frac{1}{Z_{\beta}} P(x^{t+1}|x^{t}, \delta_{i}, \beta_{i}) P(\beta_{i}|x^{1:t}, \delta_{i})$$

$$= \frac{1}{Z_{\beta}} \frac{\sqrt{V(\delta_{i})}}{2\pi (1 - \Phi(0; \mu_{\beta_{i}}^{t}, \Sigma_{\beta_{i}}^{t})) \sqrt{\Sigma_{\beta_{i}}^{t} \Sigma_{x}^{t+1}}}$$

$$\exp\left(-\frac{(\beta_{i} - \mu_{\beta_{i}}^{t})^{2}}{2\Sigma_{\beta_{i}}^{t}} - \beta_{i} V(\delta_{i}) \frac{(x^{t+1} - \mu_{x}^{t+1})^{2}}{2\Sigma_{x}^{t+1}} + \ln\sqrt{\beta_{i}}\right)$$
(15)

where $Z_{\beta} = \int P(x^{t+1}|x^t, \delta_i, \beta_i) P(\beta_i|x^{1:t}, \delta_i) d\beta_i$ is the normalization constant ensuring that the posterior $P(\beta_i|x^{1:t+1}, \delta_i)$ integrates to 1. Analytically obtaining the exact solution to (15) is intractable due to the nonlinearity inherent in the likelihood and the prior. To address this challenge, we utilize the Laplace approximation, which approximates the posterior as a normal distribution for computational efficiency [32]. The mean and covariance of the approximated posterior probability are given by

$$\mu_{\beta_i}^{t+1} = \frac{a + \sqrt{a^2 - 4b}}{2}$$

$$\Sigma_{\beta_i}^{t+1} = \left[\frac{1}{\Sigma_{\beta_i}^t} + \frac{1}{2(\mu_{\beta_i}^{t+1})^2}\right]^{-1}$$
(16)

where $a=\mu_{\beta_i}^t-V(\delta_i)\Sigma_{\beta_i}^t\frac{(x^{t+1}-\mu_x^{t+1})^2}{\Sigma_{\beta_i}^{t+1}}$, and $b=-\frac{\Sigma_{\beta_i}^t}{2}$. Then, the resulting probability distribution is truncated again to ensure that β remains within the practically valid range. The mean of the truncated normal distribution from (14) is given by

$$\bar{\mu}_{\beta_i}^{t+1} = \mu_{\beta_i}^{t+1} - \frac{\Psi\left(0; \mu_{\beta_i}^t, \Sigma_{\beta_i}^t\right)}{\Phi\left(0; \mu_{\beta_i}^t, \Sigma_{\beta_i}^t\right)} \sqrt{\Sigma_{\beta_i}^{t+1}}.$$
 (17)

Finally, based on the proximity parameter β_i and new measurement x^{t+1} , the conditional probability of potential target δ_i to be attacked is updated as follows:

$$P(\delta_{i}|x^{1:t+1}, \beta_{i}) = \frac{P(x^{t+1}|x^{t}, \delta_{i}, \beta_{i})P(\delta_{i}|x^{1:t}, \beta_{i})}{P(x^{t+1}|x^{t}, \delta_{i})}$$

$$= \frac{P(x^{t+1}|x^{t}, \delta_{i}, \beta_{i})P(\delta_{i}|x^{1:t}, \beta_{i})}{\sum_{\delta_{i}} P(x^{t+1}|x^{t}, \delta_{i}, \beta_{i})P(\delta_{i}|x^{1:t}, \beta_{i})}.$$
(18)

The probability of attack intent $P(\delta_i \mid x^{1:t+1})$ is then obtained directly from $P(\delta_i \mid x^{1:t+1}, \beta_i = \bar{\mu}_{\beta_i}^{t+1})$ and (17). The overall process of the algorithm is described in Algorithm 1.

Algorithm 1: Attack Intent Inference Algorithm.

Input Estimated state distribution $P(X^t)$,

```
Measurement x^{t+1}, Targets \delta_i \in \{\delta_1, \delta_2, \dots, \delta_{N_\delta}\},
  and Sampling Number N_s
 Output Probability of attack intent P(\delta_i|x^{1:t+1})
       for all k \leftarrow 0, 1, \dots N_s do
 1:
           Sample initial conditions from (6) and (7)
 2:
 3:
          Generate potential trajectories \tau_k using (8)
 4:
       end for
 5:
       for all i \leftarrow 0, 1, \cdots N_{\delta} do
          Identify the set of feasible trajectories \mathcal{T}_i for
          the target \delta_i using (9)
          Compute P(x^{t+1}|x^t, \delta_i) using (10)
 7:
          Compute P(x^{t+1}|x^t, \delta_i, \beta_i) using (12)
 8:
          Update P(\beta_i|x^{1:t+1}, \delta_i) using (16)
 9:
          Truncate \beta_i using (17)
Update P(\delta_i|x^{1:t+1}, \beta_i = \bar{\mu}_{\beta_i}^{t+1}) using (18).
10:
11:
```

IV. NUMERICAL SIMULATION

12:

The effectiveness of the proposed algorithm is evaluated through extensive simulations. In individual simulation scenarios, the HGV exhibits highly dynamic maneuvers, including multiple skipping and turning, and eventually strikes one of the designated targets. The proposed algorithm is demonstrated with two distinct scenarios, and further comparative, ablation studies, sensitivity analysis, and computational complexity are carried out.

A. Simulation Setup

The dynamics of HGV is modeled by (1), whose model and aerodynamic parameters are set according to the common aero vehicle-h (CAV-H) model [33]. The trajectory of HGV is then generated using the Runge–Kutta integration method based on the applied control inputs, guiding the HGV toward the designated target. Recalling (1) and (3), the control inputs consist of the angle of attack α and bank angle γ . Accounting for the physical constraints on the HGV maneuverability in practice, the profile of α is defined as a piecewise linear function of velocity, expressed as follows [34]:

$$\alpha = \begin{cases} \alpha_{\text{max}}, & v > v_1 \\ \alpha_{\text{max}} + (\alpha_{\text{L/D,max}} - \alpha_{\text{max}}) \frac{v - v_1}{v_2 - v_1}, & v_1 \leq v \leq v_2 \\ \alpha_{\text{L/D,max}}, & v < v_2 \end{cases}$$

where α_{max} is the maximum angle of attack, and $\alpha_{L/D,max}$ is the angle of attack at the maximum lift-to-drag ratio. v_1 and v_2 are velocity transition points, ensuring the HGV maintains adequate maneuverability while approaching the target. In parallel, a proportional navigation guidance law is used to adjust the bank angle γ [35]. To prevent physically infeasible maneuvers, γ and its rate of change $\dot{\gamma}$ are limited to $\gamma \in [-45^\circ, 45^\circ]$, $\dot{\gamma} \in [-2^\circ, 2^\circ]$. The detailed dynamics model and simulation parameters are summarized in Table I.

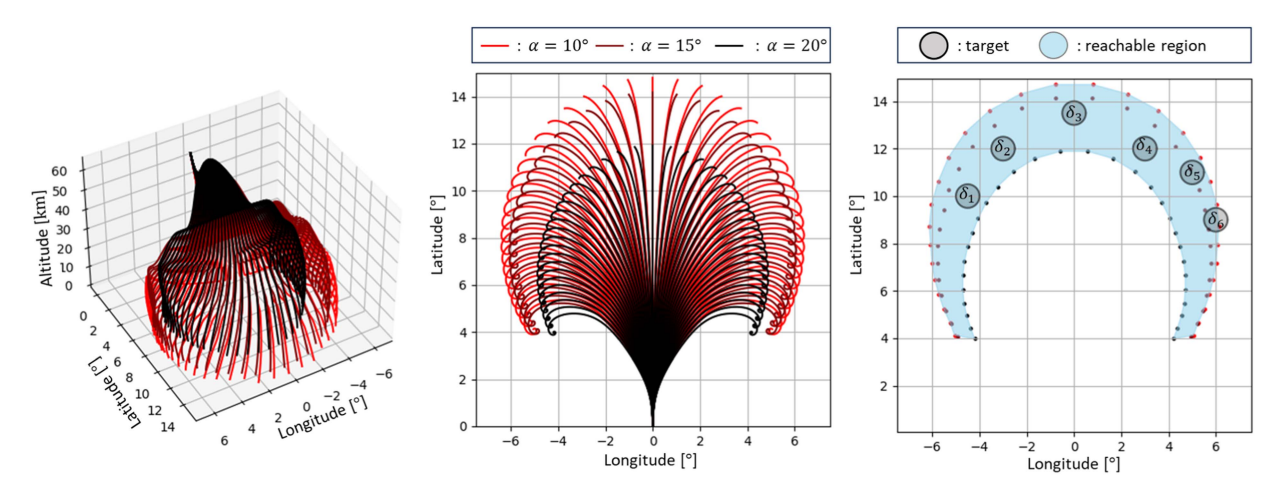


Fig. 4. Trajectories generated by varying angle of attack ($\alpha \in \{10^{\circ}, 15^{\circ}, 20^{\circ}\}$) and bank angle in 1° increments between -45° and 45° . The right plot highlights the reachable region (shaded in blue) in which the targets $\delta_i \in \{\delta_1, \ldots, \delta_{N_{\delta}}\}$, $N_{\delta} = 6$ are arbitrarily placed.

TABLE I HGV Dynamics Model and Simulation Parameters

Parameter	Description	Value
\overline{m}	Mass	907 kg
S	Reference area	$0.4839 \mathrm{m}^2$
g	Gravity	9.81 m/s^2
R_e	Earth radius	6378 km
$ ho_o$	Atmospheric density constant	$1.22~\mathrm{kg/m}^3$
α_{max}	Maximum angle of attack	20°
	Angle of attack at	10°
$lpha_{ m L/D,max}$	maximum lift-to-drag ratio	10

TABLE II Initial State of HGV

State	Value	State	Value
h_0	54–55 km	v_0	3050–3100 m/s
ϕ_0	0°	θ_0	$-0.1-0^{\circ}$
ψ_0	0°	χ_0	0-0.1°

The initial states of HGV³ are set at a certain range of gliding maneuver conditions, as outlined in Table II. Based on these initial states and the allowable ranges of the control inputs, the reachable region is first determined to ensure that target selection remains the dynamically feasible region. Fig. 4 visualizes the range of trajectory samples that can be generated from the allowable initial states and control inputs. The trace of all these samples forms the dynamically feasible region of HGV in this simulation setup. For the attack scenario specified in the next subsection, all the targets δ_i for $i \in 1, 2, \ldots, N_\delta$ are arbitrarily configured within this region. This implies the initialized HGV can reach any target, and thus fast and accurate attack intent inference is crucial for predicting its intended destination in a timely manner.

The simulations are executed on an AMD Ryzen 9 7950X 16-Core processor with 32 GB of RAM and a GeForce RTX 4090 GPU. The proposed framework is implemented using the Python library JAX to enable parallel computation on GPUs [36]. Further details on the simulation can be founded in our GitHub repository at https://github.com/HMCL-UNIST/AttackIntentInference.git.

B. Scenario Specification

Based on the above simulation setup, the simulated trajectories leading to each target are illustrated in Fig 5. The corresponding control state histories $u = [u_1, u_2, u_3]$ are plotted in Fig. 6. As noted in Section III-A, u is unknown and its estimation error is the crucial factor of dynamics uncertainty. Notably, u_3 (i.e., bank angle) exhibits abrupt variations during the flight, making the estimation significantly erroneous and impeding the subsequent trajectory prediction.

On top of these dynamics uncertainties, we further impose the different levels of uncertainties in the proposed rational decision-making model through the following two distinct scenarios.

- 1) Scenario 1: The HGV attacks the target with the highest threat value $V(\delta_i)$, whose target selection logic is well-aligned with the proposed decision-making model (i.e., low-level of uncertainty).
- 2) Scenario 2: The HGV randomly attacks a target, irrespective of the threat value $V(\delta_i)$. This scenario introduces discrepancies between the real target selection and the proposed decision-making model (i.e., high-level of uncertainty).

In the both scenarios, the threat value $V(\delta_i)$ is randomly chosen within the range $0 < V(\delta_i) \le 1$. Fig. 7(a) and (b) illustrate example trajectories and the corresponding threat values for the each simulation run of Scenario 1 and Scenario 2, respectively. In Fig. 7(a), the HGV's trajectory is directed toward the target with the highest threat value (i.e., δ_3). In contrast, Fig. 7(b) shows a case where the HGV

³In our simulation study, we do not fully simulate the trajectory of HGV from its boosting phase, but instead initialize from its gliding phase. Thus, the initial state of HGV is defined as the state when it is first observed by radar, having already transitioned into the gliding mode [8].

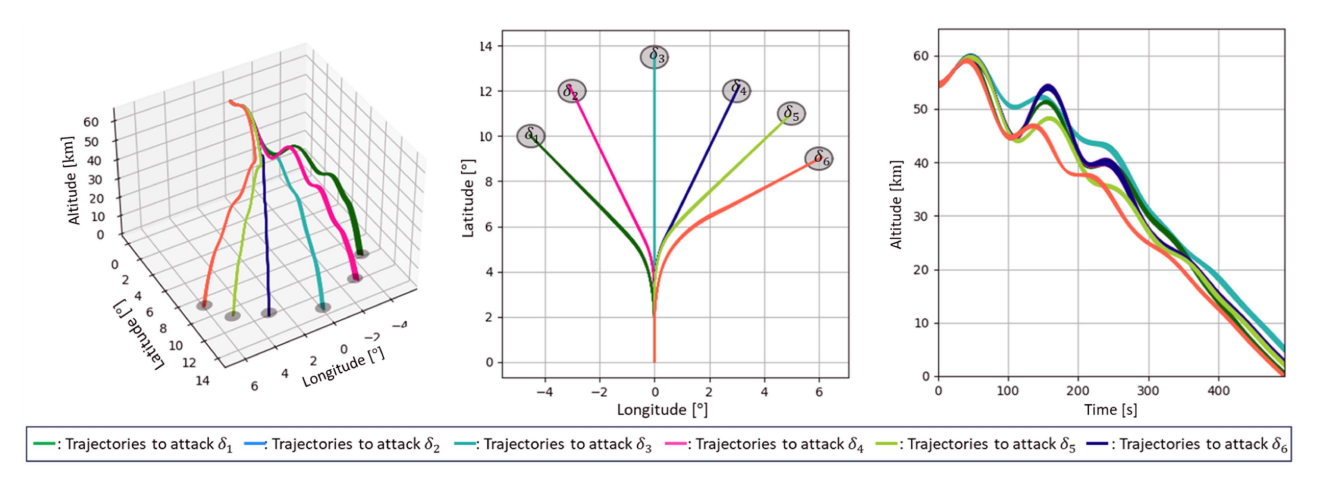


Fig. 5. Simulated trajectories of HGV navigating toward each target δ_i , $i \in \{1, 2, ..., 6\}$.

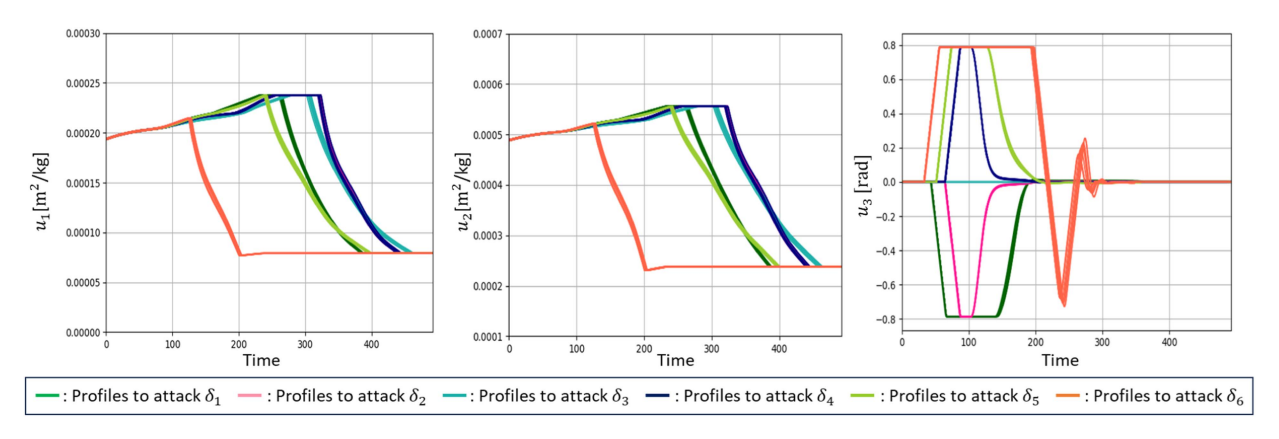


Fig. 6. Profiles of the control states u_1, u_2 , and u_3 over time while reaching each target δ_i , $i \in \{1, 2, ..., 6\}$. While u_1 and u_2 exhibit relatively small variations across the targets, u_3 shows significant difference for each target.

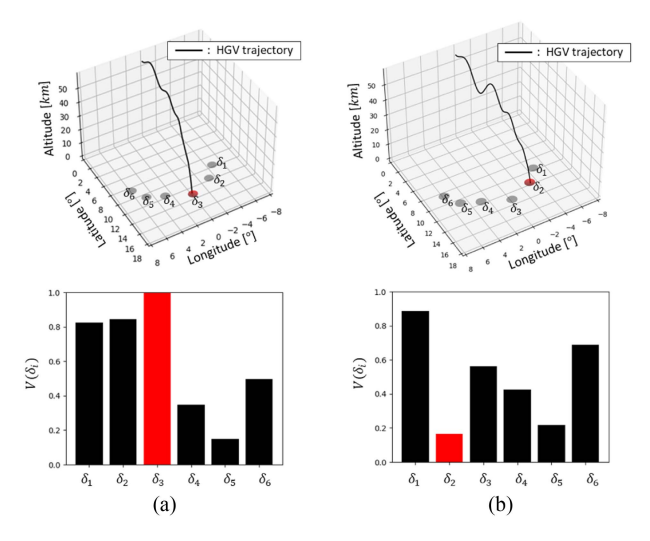


Fig. 7. Example trajectories and threat value assignments under the single HGV setting for Scenario 1 (left) and Scenario 2 (right).

attacks δ_2 despite δ_1 having the highest threat value (δ_2 is indeed the one with the lowest threat value). This may implicate two reasons for the model discrepancy: 1) the attacker may operate under internal priorities different from

the proposed decision-making model (e.g., selecting a lower threat target); or 2) the defender's specification of threat values may not accurately capture the attacker's true threat values. In either case, Scenario 2 allows us to rigorously evaluate the proposed framework under the high level of uncertainty in the decision-making model.

Besides the uncertainty level of the decision-making model, we additionally consider four operational conditions, each combined with Scenario 1 and Scenario 2, respectively, resulting in eight distinct cases as follows.

- 1) *Nominal:* The baseline setting without any variations in operational conditions.
- Data Packet Loss: This condition simulates communication dropouts by withholding measurement data during a fixed time interval.
- 3) *Sensor Failure:* This condition simulates a temporary sensor malfunction by injecting abnormally large noise into measurements.
- 4) Multi-HGV and Multitarget: This condition considers the simultaneous deployment of two HGVs, each assigned to a different target, to evaluate the scalability of the inference framework in multiagent scenarios.

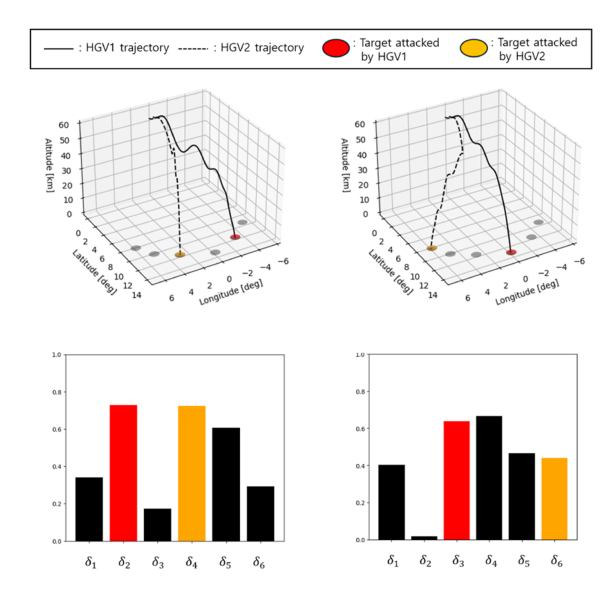


Fig. 8. Example trajectories and threat value assignments under the multi-HGV and multitarget condition for Scenario 1 (left) and Scenario 2 (right).

In the nominal case, the HGV state is assumed to be measured with Gaussian noise $\mathcal{N}(0, \sigma_n^2)$, where $\sigma_n = [5 \text{ m}, 0.0005^\circ, 0.0005^\circ, 2 \text{ m/s}, 0.05^\circ, 0.05^\circ]$ [5]. For the data packet loss and the sensor failure cases, the respective conditions are introduced between time steps 70 to 90 in the simulation, corresponding to a period of rapid bank angle transition, as shown in Fig. 6. In the data packet loss case, measurement data is completely withheld, while in the sensor failure case, measurements remain available but are subject to high sensor noise $\sigma_h = [10 \text{ m}, 0.001^\circ, 0.001^\circ, 3 \text{ m/s}, 0.1^\circ, 0.1^\circ].$

Apart from the single-HGV cases, we also consider the multi-HGV and the multitarget setting, illustrated in Fig. 8. In the Scenario 1 multi-HGV case, HGV1 is intended to attack the target with the highest threat value, while HGV2 is assigned to the second-highest target. This represents a case where the both HGVs act according to the defender's decision-making model. In contrast, the Scenario 2 multi-HGV case assumes that the both HGVs arbitrarily select their targets regardless of the defender-assigned threat values, implying the ill-posed decision-making model.

C. Algorithm Demonstration

This section demonstrates how the proposed inference algorithm operates over time based on the representative trajectories defined in the illustrative scenarios of Fig. 7(a) and (b). The proposed algorithm iteratively updates attack intent inference at each time step until the HGV reaches its target. For each step, the CKF [28] is utilized to estimate the current state of HGV using (5). Based on the estimated state and (6) and (7), $N_s = 2000$ trajectories are sampled to predict the dynamically feasible region. The prior probability of each target being attacked $P(\delta_i|x^0)$, is initially set as $1/N_{\delta}$, ensuring an equal likelihood across all potential targets at the beginning. Meanwhile, the prior distribution

of the proximity parameter is defined as a truncated normal distribution, $P(\beta_i|x^0, \delta_i) \sim T\mathcal{N}(0.5, 0.1, 0, \infty)$ [32].

Figs. 9 and 10, respectively, present a series of demonstration snapshots of the proposed algorithm. The individual snapshots illustrate the progression of dynamics-based trajectory propagation and attack intent inference using the unified dynamics and decision-making model. The top row in Figs. 9 and 10 visualizes the dynamically feasible region (shaded in yellow), along with sampled trajectories leading to the potential targets. Correspondingly, the bottom row displays the probability of each target being attacked, whereas the red color indicates the actual target to be attacked by the HGV.

During the early stages of the simulation, it is dynamically feasible for the HGV to attack any of the potential targets, resulting in a broad feasible region. However, the proposed algorithm compensates for this by incorporating the decision-making model with threat value $V(\delta_i)$ to infer the attack intent. As a result, in the low uncertainty scenario where the HGV attacks the target with the highest threat value (Scenario 1), Fig. 9 shows that the probability assigned to the actual target rapidly increases over time. Conversely, in the high uncertainty scenario where the HGV attacks a target randomly (Scenario 2), Fig. 10 shows that the probabilities of each target being attacked are relatively dispersed for a while, reflecting a discrepancy between the model and observed behavior. Nevertheless, the proximity parameter β mitigates this uncertainty by progressively refining the probability distribution, as formulated in (12). Hence, despite the high uncertainty, the proposed algorithm successfully adapts to the uncertain HGV behaviors, ensuring reliable attack intent inference.

For a more comprehensive evaluation of the proposed algorithm, four analyses are carried out in the following subsections.

- 1) *Comparative Study* evaluates the performance of attack intent inference in comparison to the two existing methods [7], [19].
- 2) *Ablation Study* examines the effectiveness of the proximity parameters against the uncertainties in the dynamics and the decision-making models.
- 3) *Sensitivity Analysis* investigates the impact of varying key parameters on inference performance.
- 4) Computational Complexity assesses the runtime efficiency of the proposed framework.

D. Comparative Study

The comparative study performs the same simulation scenarios with the two existing baseline methods: 1) the dynamics-based prediction [7]; and 2) the planning-based prediction [19]. Their detailed mechanisms are described as follows.

Dynamics-Based Prediction [7]: This method propagates potential trajectories from the current estimated state and identifies those that are terminated

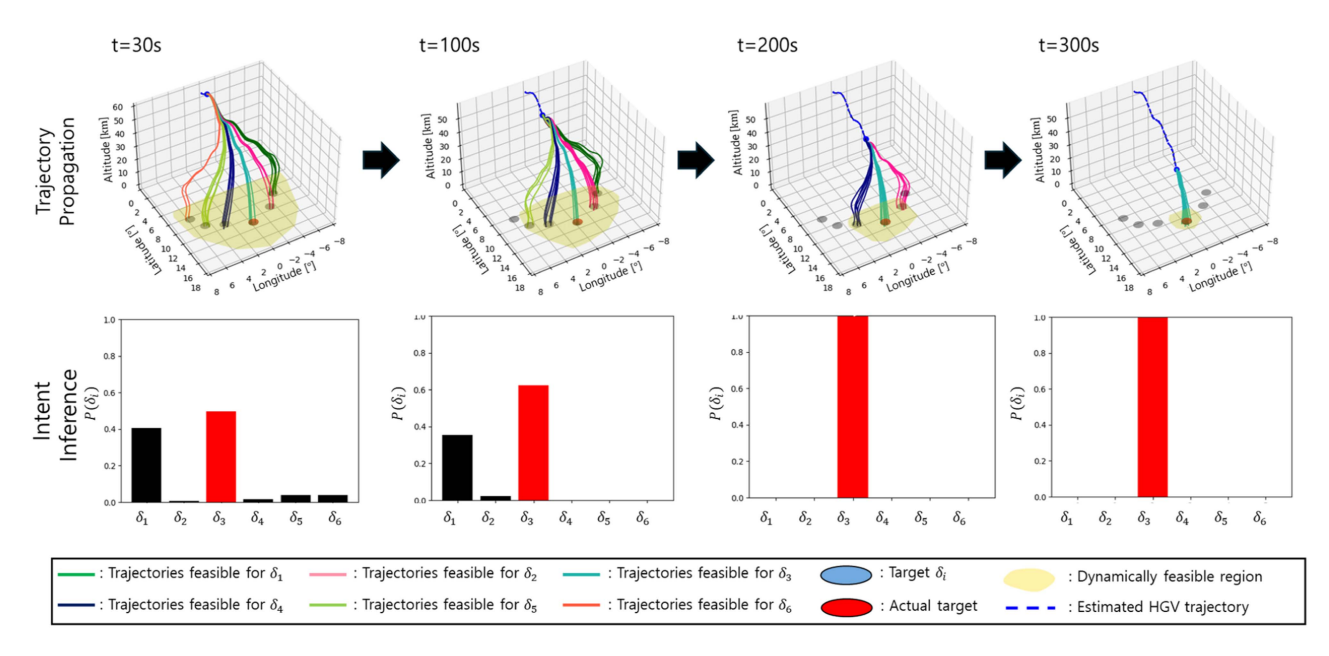


Fig. 9. Snapshots of the proposed attack intent inference framework over time in Scenario 1.

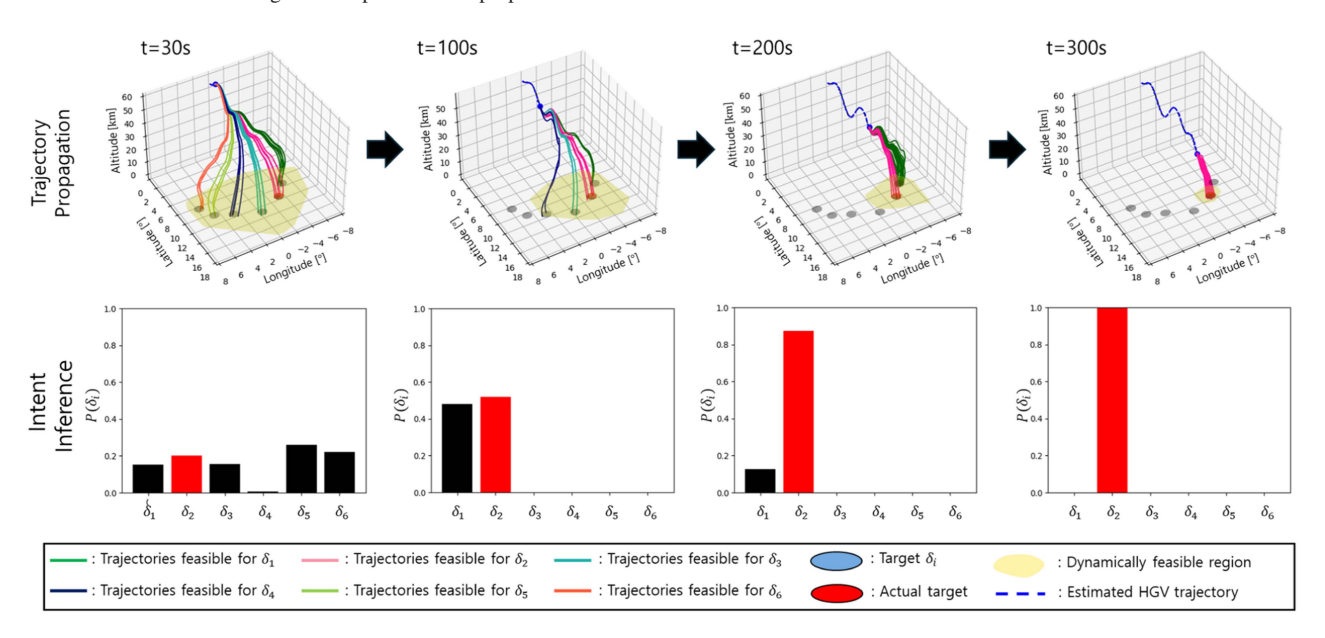


Fig. 10. Snapshots of the proposed attack intent inference framework over time in Scenario 2.

- within the target region $R(\delta_i)$. The attack intent is inferred by calculating the fraction of these trajectories relative to the total number of generated trajectories.
- 2) Planning-Based Prediction [19]: This method encodes the HGV's attack intent into a rational decision-making model under the premise that it maximizes the threat value while following the shortest path to the target. Based on this decision-making model, the algorithm defines the state transition probability as follows:

$$P(x^{t+1}|x^t, \delta_i)$$

$$\sim \exp(a \cdot d_{\text{distance}} + b \cdot d_{\text{head}} - c \cdot V(\delta_i))$$

where a, b, and c are weighting factors, d_{distance} gauges the change in the HGV-target distance along the shortest path, while d_{head} measures the angular deviation between the HGV's heading and the direction toward the target.

The proposed inference framework is compared against the above two existing methods across the eight distinct cases, covering all the combinations of the two decision-making scenarios and the four operational conditions. Each method is evaluated over 300 independent simulation runs per case. The main results under nominal condition are presented in Figs. 11 and 12 and Table III. Figs. 11 and 12 plot attack intent inference performance over time, i.e.,

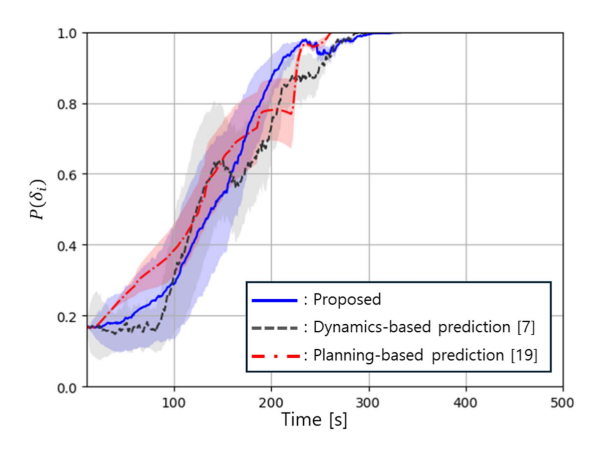


Fig. 11. Intent inference performance analysis for Scenario 1 - Nominal (Solid lines are mean values of the target probability and shaded areas are the corresponding variances).

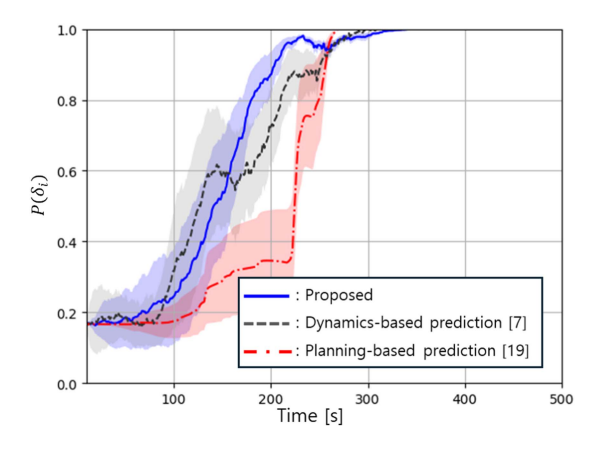


Fig. 12. Intent inference performance analysis for Scenario 2 - Nominal (Solid lines are mean values of the target probability and shaded areas are the corresponding variances).

TABLE III
Inference Time and Success Rate Analysis for Nominal Condition

	Scenario 1		Scenario 2	
	Inference	Success	Inference	Success
	Time [s]	Rate [%]	Time [s]	Rate [%]
Proposed	184.72	89.6	184.19	87.8
Proposed without β	224.87	81.0	233.78	76.3
Dynamic-based prediction [7]	224.15	83.3	226.22	84.6
Planning-based prediction [19]	187.85	88.4	222.67	79.25

the probability update statistics of the target being attacked (mean and variance). Table III presents the performance comparisons of the methods with respect to two relevant measures:

- 1) *Inference Time:* the time elapsed until the correct inference made, i.e., the probability of the actual target exceeds a high enough threshold (0.9 in our set-up), indicating the speed of inference convergence; and
- Success Rate: the rate of correct inference made before the HGV descends below a low enough altitude threshold.

In particular, since prediction during skipping maneuvers is hardly tractable due to rapid trajectory changes [9], the success rate is evaluated at the point when the skipping

TABLE IV
Inference Time and Success Rate Analysis for Data Packet Loss
Condition

	Scenario 1		Scenario 2	
	Inference	Success	Inference	Success
	Time [s]	Rate [%]	Time [s]	Rate [%]
Proposed	194.19	87.8	189.4	88.3
Proposed without β	232.37	74.0	237.87	74.7
Dynamic-based prediction [7]	226.62	84.0	221.26	82.3
Planning-based prediction [19]	194.7	89.7	232.18	75.4

maneuver concludes, typically at an altitude of 35 km in our setup (See Fig. 5). A high success rate signifies both the accuracy of the prediction and its practical implication, as a successful inference under these conditions would facilitate effective interceptor engagement.

As seen in Table III, the dynamics-based prediction [7] converges at approximately 230 s in both scenarios. This relatively slower convergence can be attributed to the lack of consideration to the decision-making model, which limits its ability to take notice of the different threat values of the targets. Furthermore, as illustrated in Fig. 6, the bank angle undergoes dramatic changes around 100 s, introducing significant uncertainty into the estimated state. This uncertainty eventually degrades the inference performance, leading to reduced success rates. Consequently, the dynamics-based approach struggles to maintain reliable prediction in scenarios involving the high maneuverability of HGV.

On the other hand, the planning-based prediction [19] overly relies on the threat value $V(\delta_i)$ for its decision-making process. While this dependency allows it to perform adequately when the actual target agrees with the highest threat value (Scenario 1), it significantly limits its adaptability in the random target scenario (Scenario 2). As shown in Table III, the planning-based method in Scenario 2 significantly degrades in both inference time and success rate, compared to Scenario 1. Furthermore, the dynamics information considered in this method merely accounts for the shortest path to the target, lacking insight into dynamically feasible trajectories. Consequently, during the early stages of the simulation, the inference exhibits significant variance depending on the target location.

In contrast, the proposed algorithm overcomes the limitations of the existing methods by effectively integrating the dynamics and the decision-making model, enabling faster and more accurate attack inference. In addition, the proximity parameter effectively handles dynamical uncertainties and the potential discrepancy from the rational decision-making model, ensuring reliable performance across scenarios with varying uncertainty levels. As a result, the proposed algorithm demonstrates a steady and progressive increase in the target probability over time regardless of uncertainty levels, as illustrated in Figs. 11 and 12. Furthermore, it achieves faster convergence and higher accuracy compared to existing baselines, as shown in Table III.

These advantages become even more pronounced under adversarial operational conditions. Table IV presents the results under data packet loss, and Table V shows performance

TABLE V
Inference Time and Success Rate Analysis for Sensor Failure Condition

	Scenario 1		Scenario 2	
	Inference	Success	Inference	Success
	Time [s]	Rate [%]	Time [s]	Rate [%]
Proposed	189.33	88.8	191.2	87.8
Proposed without β	246.7	70.7	247.64	71.3
Dynamic-based prediction [7]	236.26	82.8	238.22	79.9
Planning-based prediction [19]	183.6	87.9	234.06	77.7

TABLE VI Inference Time and Success Rate Analysis Under the Multi-HGV and Multitarget Condition in Scenario 1

	HGV1		HGV2	
	Inference	Success	Inference	Success
	Time [s]	Rate [%]	Time [s]	Rate [%]
Proposed	185.54	90.9	184.72	86.3
Proposed without β	223.8	78.5	237.81	76.0
Dynamic-based prediction [7]	232.85	82.8	246.22	78.2
Planning-based prediction [19]	190.4	87.3	223.5	82.4

TABLE VII
Inference Time and Success Rate Analysis Under the Multi-HGV and
Multitarget Condition in Scenario 2

	HGV1		HGV2	
	Inference	Success	Inference	Success
	Time [s]	Rate [%]	Time [s]	Rate [%]
Proposed	189.88	90.3	188.86	88.8
Proposed without β	233.68	75.0	234.45	75.8
Dynamic-based prediction [7]	232.77	82.8	245.2	78.8
Planning-based prediction [19]	233.02	78.5	238.24	72.9

under sensor failure. In the both cases, the inference time of the proposed method slightly increases due to the extra operational uncertainties. Nevertheless, it consistently outperforms the dynamics-based and planning-based methods in terms of both inference accuracy and reliability.

Lastly, Tables VI and VII highlight the scalability of the proposed framework in the multi-HGV inference. The results demonstrate that the proposed framework consistently achieves a high success rate while maintaining lower inference times compared to the existing methods, regardless of which HGV intends to attack which target. Similar to the single-HGV condition, the planning-based method shows strong dependency on the threat values. Consequently, when another HGV is assigned to a relatively lower threat target as in the case of HGV2 in Scenario 1, its inference performance degrades significantly, revealing its limited adaptability in the multi-HGV condition. In contrast, the proposed algorithm accounts for the potential discrepancy in the attacker's decision-making model, and thus can robustly cope with multi-HGV conditions without requiring any substantial modification.

E. Ablation Study

To further examine the role of the proximity parameter on the proposed intent inference framework, an ablation study is conducted by comparing the full proposed method with a modified version where the proximity parameter β is excluded from (12)

$$P(x^{t+1}|x^t, \delta_i) \sim \exp\left(V(\delta_i) \cdot \frac{(x^{t+1} - \mu_x^{t+1})^2}{2\Sigma_x^{t+1}}\right).$$

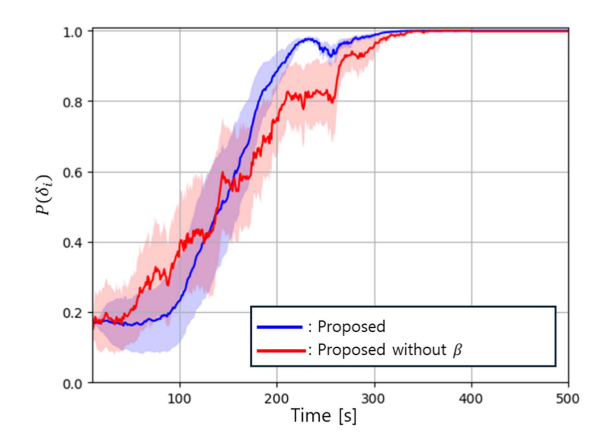


Fig. 13. Intent inference performance analysis for Scenario 1 - Nominal (Solid lines are mean values of the target probability and shaded areas are the corresponding variances).

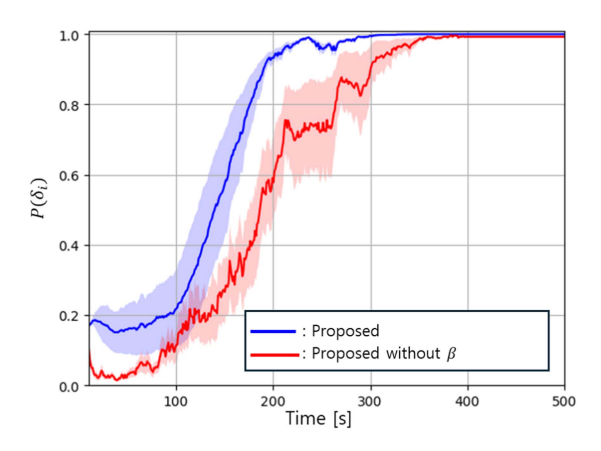


Fig. 14. Intent inference performance analysis for Scenario 2 - Nominal (Solid lines are mean values of the target probability and shaded areas are the corresponding variances).

Each method is evaluated over 300 simulation runs across the eight cases, as described in Section IV-B. The results under nominal conditions are summarized in Figs. 13 and 14, as well as Tables III. As shown in the results, the proposed method demonstrates smoother and faster convergence compared to the ablated model. It is prominent that the absence of the proximity parameter yields more variability of the inference in the early stage of simulation. Moreover, the results subject to the other operational conditions (See Tables IV–VII) consistently highlight the effectiveness of the proximity parameter. These results underscore the critical role of the proximity parameter in handling the uncertainties inherent in the decision-making model.

F. Sensitivity Analysis

Building on the previous analysis, we further assess the robustness of the proposed framework by conducting a sensitivity analysis. As defined in (12), the proposed model depends on three elements: 1) measurement noise $\mathcal{N}(0, \sigma^2)$; 2) threat value $V(\delta_i)$; and 3) proximity parameter β_i . Among these, σ and $V(\delta_i)$ are externally specified parameters, whereas β_i is an internally estimated parameter

TABLE VIII

Inference Performance Under Varying Measurement Noise Levels for Scenario 1

	Inference Time [s]	Success Rate [%]	Inferred β
Nominal noise setting (σ_n)	184.72	89.6	0.00147
Higher noise setting (σ_h)	207.40	82.5	0.00094

TABLE IX

Inference Performance Under Varying Measurement Noise Levels for Scenario 2

	Inference Time [s]	Success Rate [%]	Estimated β
Nominal noise setting (σ_n)	184.19	87.8	0.00321
Higher noise setting (σ_h)	212.70	82.9	0.00160

TABLE X

Inference Performance and Estimated β Under Varying Threat Value Ranges for Scenario 1

Threat Range	Inference Time [s]	Success Rate [%]	Estimated β
$0 < V(\delta) \le 1$	184.72	89.6	0.00147
$0 < V(\delta) \le 10$	190.02	86.7	0.00017
$0 < V(\delta) \le 100$	198.44	81.0	0.00001

TABLE XI

Inference Performance and Estimated β Under Varying Threat Value Ranges for Scenario 2

	Inference Time [s]	Success Rate [%]	Inferred β
$0 < V(\delta) \le 1$	184.19	87.8	0.00367
$0 < V(\delta) \le 10$	190.89	87.0	0.00054
$0 < V(\delta) \le 100$	183.35	84.5	0.00001

through the Bayesian inference process (13). Accordingly, to conduct a fair sensitivity analysis, we vary the external parameters σ and $V(\delta_i)$, and evaluate the susceptibility in inference performance and the estimated β_i . Specifically, the following two variations are tested for the sensitivity analysis purpose.

- 1) Measurement Noise Level Variation: We compare the nominal noise setting $\sigma_n = [5 \text{ m}, 0.0005^\circ, 0.0005^\circ, 2\text{m/s}, 0.05^\circ, 0.05^\circ]$ with the higher noise setting $\sigma_h = [10 \text{ m}, 0.001^\circ, 0.001^\circ, 3\text{m/s}, 0.1^\circ, 0.1^\circ].$
- 2) Threat Value Variation:⁴ We evaluate three distinct ranges of threat values, namely $0 < V(\delta_i) \le 1$, $0 < V(\delta_i) \le 10$, and $0 < V(\delta_i) \le 100$.

The above variations are, respectively, applied to Scenario 1 and Scenario 2, under the nominal operational condition. All simulations are conducted over 300 independent runs. Tables VIII and IX present the results under varying noise levels for each scenario. As expected, inference performance degrades with respect to increasing measurement noise. In addition, Tables X and XI summarize the algorithm's sensitivity to the threat value variation. As the range of threat values increases, inference performance gradually degenerates due to amplified discrepancy between the considered decision-making model and the HGV observed behavior.

Although inference performance inevitably degrades under higher uncertainty, the proximity parameter helps

TABLE XII

Average Execution Time Per Time Step With Respect to Different Numbers of MC Samples

	500	1000	1500	2000
		0.0174s		
PC 2	0.0206s	0.0208s	0.0217s	0.0232s

TABLE XIII

Inference Time and Success Rate With Respect to Different Numbers of MC Samples

	500	1000	1500	2000
Inference Time [s]	205.19	195.94	188.5	184.72
Success Rate [%]	87.67	89.2	89.2	89.6

mitigate this degradation by compensating for variations in measurement noise and target value. This mechanism is evidently observed in the estimated proximity parameter β , which consistently decreases under both higher noise levels and broader threat value ranges. From the properly adjusted β estimate, the downstream Bayesian update robustifies the inference quality under external uncertainty.

G. Computational Complexity

Finally, we evaluate the algorithm execution time versus inference performance by varying numbers of MC trajectory samples to examine the computational efficiency and real-time applicability. First, the average execution time per time step is evaluated across two computing platforms: 1) the default experimental platform (PC 1: Ryzen 9 7950X, RTX 4090); and 2) a lower spec platform (PC 2: i5-12600KF, RTX 3070). As shown in Table XII, both platforms demonstrate comparable computing performance. Even with 2000 MC samples, the execution time per time step remains below 25 ms, corresponding to a 40–50-Hz update rate. Considering that typical missile defense systems' measurement update rate is around 1 Hz [8], the proposed framework successfully fulfills real-time operational requirements.

Second, Table XIII presents the overall inference time and success rate in Scenario 1 with respect to the different numbers of MC samples, ranging from 500–2000. Here, the inference performance improves up to 1500 samples, but shows marginal improvement beyond that number. More importantly, such marginal performance is achieved without any issue in computation overhead, i.e., the update rate is well above 1 Hz. Thus, the proposed algorithm can be deployed in real-time applications without imposing a significant tradeoff between computational efficiency and inference performance.

V. CONCLUSION

This article presents an attack intent inference framework to predict the potential attack target of the HGV. First, a unified dynamics and decision-making model is developed to accommodate both the dynamical feasibility and tactical objectives of the HGV behaviors. Within this model, the HGV probabilistically seeks the target that yields the highest threat value in dynamically feasible regions,

⁴In practice, threat values are often normalized within the range [0,1] [37], whereby the excessive threat value variation can be mitigated.

fulfilling rational decision-making. Coping with uncertainties and model discrepancies arising in real-world, the proposed framework incorporates a proximity parameter. This parameter, alongside the potential attack target, is then inferred using the Bayesian approach, which efficiently updates the probability of attack intent. Numerical simulations demonstrated the effectiveness of the proposed method, showing higher accuracy and faster convergence in inferring the HGV's attack intent. Future work may extend this framework toward a comprehensive decision-making architecture capable of modeling intricate attack strategies in multi-HGV scenarios.

REFERENCES

- [1] D. Yibo, Y. Xiaokui, C. Guangshan, and S. Jiashun, "Review of control and guidance technology on hypersonic vehicle," *Chin. J. Aeronaut.*, vol. 35, no. 7, pp. 1–18, 2022.
- [2] E. R. Bartusiak, M. A. Jacobs, M. W. Chan, M. L. Comer, and E. J. Delp, "Predicting hypersonic glide vehicle behavior with stochastic grammars," *IEEE Trans. Aerosp. Electron. Syst.*, vol. 60, no. 1, pp. 1208–1223, Feb. 2024.
- [3] M. Li, C. Zhou, L. Shao, H. Lei, and C. Luo, "Intelligent trajectory prediction algorithm for reentry glide target based on intention inference," *Appl. Sci.*, vol. 12, no. 21, 2022, Art. no. 10796.
- [4] F. Li, J. Xiong, Z. Qu, and X. Lan, "A damped oscillation model for tracking near space hypersonic gliding targets," *IEEE Trans. Aerosp. Electron. Syst.*, vol. 55, no. 6, pp. 2871–2890, Dec. 2019.
- [5] J. Huang, Z. Li, D. Liu, Q. Yang, and J. Zhu, "An adaptive state estimation for tracking hypersonic glide targets with model uncertainties," *Aerosp. Sci. Technol.*, vol. 136, 2023, Art. no. 108235.
- [6] Y. Fan, W. Zhu, and G. Bai, "A cost-effective tracking algorithm for hypersonic glide vehicle maneuver based on modified aerodynamic model," *Appl. Sci.*, vol. 6, no. 10, 2016, Art. no. 312.
- [7] Y. Hu, C. Gao, J. Li, and W. Jing, "Maneuver mode analysis and parametric modeling for hypersonic glide vehicles," *Aerosp. Sci. Technol.*, vol. 119, 2021, Art. no. 107166.
- [8] J. Ren, X. Wu, Y. Liu, F. Ni, Y. Bo, and C. Jiang, "Long-term trajectory prediction of hypersonic glide vehicle based on physicsinformed transformer," *IEEE Trans. Aerosp. Electron. Syst.*, vol. 59, no. 6, pp. 9551–9561, Dec. 2023.
- [9] G. Li, H. Zhang, and G. Tang, "Maneuver characteristics analysis for hypersonic glide vehicles," *Aerosp. Sci. Technol.*, vol. 43, pp. 321–328, 2015.
- [10] C. Han and J. Xiong, "Method of trajectory prediction for unpowered gliding hypersonic vehicle in gliding phase," in *Proc. IEEE Adv. Inf. Manage., Commun., Electron. Automat. Control Conf.*, 2016, pp. 262–266.
- [11] Y. Hu, Z. Liu, C. Jiang, W. Jing, and C. Gao, "Maneuver mode parametric modeling based on trajectory curve evolution laws for hypersonic glide vehicles," *Aerosp. Sci. Technol.*, vol. 157, 2024, Art. no. 109856.
- [12] S. Hochreiter, "Long short-term memory," Neural Computation, vol. 9, no. 8, pp. 1735–1780, Nov. 1997.
- [13] H. Xu, Y. Liu, Y. Xing, A. Ren, and Y. Quan, "Lateral maneuver discrimination for hypersonic glide vehicles: A hybrid approach combining model-driven and data-driven methods," *IEEE Sensors* J., vol. 24, no. 7, pp. 11425–11437, Apr. 2024.
- [14] J. Zhang, J. Xiong, L. Li, Q. Xi, X. Chen, and F. Li, "Motion state recognition and trajectory prediction of hypersonic glide vehicle based on deep learning," *IEEE Access*, vol. 10, pp. 21095–21108, 2022.
- [15] M. Li, C. Zhou, L. Shao, and H. Lei, "An intelligent trajectory prediction algorithm for hypersonic glide targets based on maneuver mode identification," *Int. J. Aerosp. Eng.*, vol. 2022, no. 1, 2022, Art. no. 4625001.

- [16] J. L. Yepes, I. Hwang, and M. Rotea, "New algorithms for aircraft intent inference and trajectory prediction," *J. Guidance, Control, Dyn.*, vol. 30, no. 2, pp. 370–382, 2007.
- [17] F. Teng, X. Guo, Y. Song, and G. Wang, "An air target tactical intention recognition model based on bidirectional GRU with attention mechanism," *IEEE Access*, vol. 9, pp. 169122–169134, 2021.
- [18] M. Guanglei, Z. Runnan, W. Biao, Z. Mingzhe, W. Yu, and L. Xiao, "Target tactical intention recognition in multiaircraft cooperative air combat," *Int. J. Aerosp. Eng.*, vol. 2021, no. 1, 2021, Art. no. 9558838.
- [19] Y. Hu, C. Gao, J. Li, W. Jing, and Z. Li, "Novel trajectory prediction algorithms for hypersonic gliding vehicles based on maneuver mode on-line identification and intent inference," *Meas. Sci. Technol.*, vol. 32, no. 11, 2021, Art. no. 115012.
- [20] D. Fridovich-Keil et al., "Confidence-aware motion prediction for real-time collision avoidance," *Int. J. Robot. Res.*, vol. 39, no. 2/3, pp. 250–265, 2020.
- [21] J. Xu, C. Dong, and L. Cheng, "Deep neural network-based footprint prediction and attack intention inference of hypersonic glide vehicles," *Mathematics*, vol. 11, no. 1, 2022, Art. no. 185.
- [22] J. Zhang, J. Xiong, X. Lan, Y. Shen, X. Chen, and Q. Xi, "Trajectory prediction of hypersonic glide vehicle based on empirical wavelet transform and attention convolutional long short-term memory network," *IEEE Sensors J.*, vol. 22, no. 5, pp. 4601–4615, Mar. 2022.
- [23] F. Liu, L. Lu, Z. Zhang, Y. Xie, and J. Chen, "Intelligent trajectory prediction algorithm for hypersonic vehicle based on sparse associative structure model," *Drones*, vol. 8, no. 9, 2024, Art. no. 505.
- [24] B. D. Ziebart et al., "Maximum entropy inverse reinforcement learning," in *Proc. AAAI Conf. Artif. Intell.*, Chicago, IL, USA, 2008, pp. 1433–1438.
- [25] C. L. Baker, J. B. Tenenbaum, and R. R. Saxe, "Goal inference as inverse planning," in *Proc. Annu. Meeting Cogn. Sci. Soc.*, 2007, pp. 779–784.
- [26] S. Levine and V. Koltun, "Continuous inverse optimal control with locally optimal examples," in *Proc. 29th Int. Conf. Int. Conf. Mach. Learn.*, Omnipress, Madison, WI, USA, 2012, pp. 475–482.
- [27] K. An, Z.-Y. Guo, X.-P. Xu, and W. Huang, "A framework of trajectory design and optimization for the hypersonic gliding vehicle," *Aerosp. Sci. Technol.*, vol. 106, 2020, Art. no. 106110.
- [28] I. Arasaratnam and S. Haykin, "Cubature Kalman filters," *IEEE Trans. Autom. Control*, vol. 54, no. 6, pp. 1254–1269, 2009.
- [29] R. M. Neal, "Slice sampling," Ann. Statist., vol. 31, no. 3, pp. 705–767, 2003.
- [30] F. Argenti, G. Landucci, G. Spadoni, and V. Cozzani, "The assessment of the attractiveness of process facilities to terrorist attacks," Saf. Sci., vol. 77, pp. 169–181, 2015.
- [31] S. M. Lynch, Introduction to Applied Bayesian Statistics and Estimation for Social Scientists, vol. 1. Berlin, Germany: Springer, 2007.
- [32] Y. Nam and C. Kwon, "Active inference-based planning for safe human-robot interaction: Concurrent consideration of human characteristic and rationality," *IEEE Robot. Automat. Lett.*, vol. 9, no. 8, pp. 7086–7093, Aug. 2024.
- [33] T. R. Jorris, "Common aero vehicle autonomous reentry trajectory optimization satisfying waypoint and no-fly zone constraints," Ph.D. Dissertation, Dept. Aeronaut. Astronaut., Air Force Inst. Technol., Wright-Patterson AFB, OH, USA, 2007.
- [34] W. Sun, P. Ma, S. Wang, and T. Chao, "Analytical solutions for hypersonic glide trajectory based on altitude-velocity profile," *IEEE Trans. Aerosp. Electron. Syst.*, vol. 60, no. 5, pp. 7423–7436, Oct. 2024.
- [35] J. Wang and R. Zhang, "Terminal guidance for a hypersonic vehicle with impact time control," *J. Guidance, Control, Dyn.*, vol. 41, no. 8, pp. 1790–1798, 2018.
- [36] J. Bradbury et al., "JAX: Composable transformations of python NumPy programs," 2018. [Online]. Available: https://github.com/ google/jax
- [37] F. Johansson and G. Falkman, "A Bayesian network approach to threat evaluation with application to an air defense scenario," in *Proc.* 11th Int. Conf. Inf. Fusion, 2008, pp. 1–7.



Youngim Nam (Graduate Student Member, IEEE) received the B.S. degree in mechanical engineering, in 2020, from the Ulsan National Institute of Science and Technology, Ulsan, South Korea, where she is currently working toward the Ph.D. degree in mechanical engineering.

Her research interests include human-robot interaction, intent inference, and uncertainty-aware planning.



Hojin Lee (Student Member, IEEE) received the B.S. degree in electronics engineering from Macquarie University, Sydney, NSW, Australia, in 2018. He is currently working toward the Ph.D. degree in mechanical engineering with the Ulsan National Institute of Science and Technology, Ulsan, South Korea.

His research interests include autonomous mobility systems, encompassing planning under uncertainty, distributed multiagent systems, and advanced learning-based control and estimation.



Hyoekjin Choi (Member, IEEE) received the M.S. degree in computer science from Dongguk University, Seoul, South Korea, in 1995.

He is currently a Principal Researcher with the Korea Agency for Defense and Development, Daejeon, South Korea. His research interests include ballistic missile defense and command and control systems using artificial intelligence.



Won-sang Ra (Member, IEEE) received the B.S. degree in electrical engineering, the M.S. degree in electrical and computer engineering, and the Ph.D. degree in electrical and electronic engineering from Yonsei University, Seoul, South Korea in 1998, 2000, and 2009, respectively.

From 2000 to 2009, he was with the Guidance and Control Department, Agency for Defense Development, Daejeon, South Korea, as a Senior Researcher. Since 2009, he has been with the

School of Mechanical and Control Engineering, Handong Global University, Pohang, South Korea, where he is currently a Professor. From 2022 to 2023, he collaborated as a visiting Professor with the School of Aerospace, Transport, and Manufacturing, Cranfield University, Cranfield, U.K. His research interests include robust filtering theory and its applications to autonomous vehicle guidance, control, and sensor fusion.



Cheolhyeon Kwon (Member, IEEE) received the B.S. degree in aerospace engineering from Seoul National University, Seoul, South Korea, in 2010, and the M.S. and Ph.D. degrees in aeronautics and astronautics from Purdue University, West Lafayette, IN, USA, in 2013 and 2017, respectively.

He is currently an Associate Professor with the Department of Mechanical Engineering, UNIST, Ulsan, South Korea, and the Director of the High-assurance Mobility Control labora-

tory. His research interests include control and estimation for dynamical cyber-physical systems (CPS), networked intelligent autonomy, and multiagent system networks. His research goal is to pursue high-assurance CPS design through the lens of control and estimation theory foundation, with applications to systems with mobility, such as autonomous driving, advanced air mobility, etc.